# Shaping the infrared luminescence of colloidal nanocrystals using a dielectric microcavity

Erwan Bossavit, Huichen Zhang, Nicolas Ledos, Mariarosa Cavallo, Dario Mastrippolito, Leonardo Curti, Adrien Khalili, Albin Colle, Pierrick Lample, Mateusz Weis, et al.

▶ **To cite this version:**

Erwan Bossavit, Huichen Zhang, Nicolas Ledos, Mariarosa Cavallo, Dario Mastrippolito, et al.. Shaping the infrared luminescence of colloidal nanocrystals using a dielectric microcavity. Advanced Functional Materials, 2024, 10.1002/adfm.202403532 . hal-04541939

**HAL Id: hal-04541939**
**https://hal.science/hal-04541939**

Submitted on 11 Apr 2024

**HAL** is a multi-disciplinary open access archive for the deposit and dissemination of scientific research documents, whether they are published or not. The documents may come from teaching and research institutions in France or abroad, or from public or private research centers.

L'archive ouverte pluridisciplinaire **HAL**, est destinée au dépôt et à la diffusion de documents scientifiques de niveau recherche, publiés ou non, émanant des établissements d'enseignement et de recherche français ou étrangers, des laboratoires publics ou privés.

Distributed under a Creative Commons Attribution - NonCommercial 4.0 International License

# Shaping the infrared luminescence of colloidal nanocrystals using a dielectric microcavity

Erwan Bossavit[1,2$], Huichen Zhang[1$], Nicolas Ledos[1], Mariarosa Cavallo[1], Dario Mastrippolito[1], Leonardo Curti[3], Adrien Khalili[1], Albin Colle[1], Pierrick Lample[4,5] Mateusz Weis[4], Florent Margaillan[1], Xavier Lafosse[6], Yoann Prado[1], Emmanuel Péronne[4], Debora Pierucci[1], Sandrine Ithurria[3], Davide Boschetto[4], Benjamin T. Diroll[7], Aloyse Degiron[8], Emmanuel Lhuillier[1*]

[1] Sorbonne Université, CNRS, Institut des NanoSciences de Paris, INSP, F-75005 Paris, France.
[2] Synchrotron SOLEIL, L'Orme des Merisiers, Départementale 128, 91190 Saint-Aubin, France.
[3] Laboratoire de Physique et d'Etude des Matériaux, ESPCI-Paris, PSL Research University, Sorbonne Université, CNRS UMR 8213, 10 rue Vauquelin 75005 Paris, France.
[4] LOA, ENSTA Paris, Ecole Polytechnique, CNRS, Institut Polytechnique de Paris, 181 Chemin de la Hunière et des Joncherettes 91120 Palaiseau, France.
[5]Université Paris-Saclay, CEA, CNRS, LIDYL, Gif-sur-Yvette, 91191, France
[6]Centre de Nanosciences et de Nanotechnologies, CNRS, Université Paris-Saclay, C2N, Palaiseau 2110, France.
[7] Center for Nanoscale Materials, Argonne National Laboratory, 9700 S. Cass Avenue, Lemont, Illinois 60439, United States.
[8] Université de Paris, CNRS, Laboratoire Matériaux et Phénomènes Quantiques, 75013 Paris, France.

$ these two authors have equal contributions

*To whom correspondence should be sent: el@insp.upmc.fr

**Abstract:** As they gained maturity, colloidal nanocrystals also expand the spectral range of which they can be used for photonic and optoelectronic applications. In particular infrared use of nanocrystals become of utmost interest to develop alternatives cost effective to current technologies. It is then central not to let the material dictate the light matter interaction and this why the coupling of nanocrystal to photonic cavity has been explored. For infrared NCs, this approach has first been devoted to the control of absorption with in mind the increased of absorption magnitude for detector. Lots of effort have been focused on the use of metallic metasurface which also generate significant optical losses and possible quenching of the exciton. Here, we rather focus on the coupling of infrared nanocrystals to dielectric mirror cavity. We use HgTe/CdS core shell and integrated into a cavity made of aperiodic dielectric mirror. We systematically studied the effect of the substrate on spectral linewidth, carrier dynamic and emission directivity. Cavity is shown to narrow the PL by a factor 10, while focusing emission over a 12° angle. Monitoring the power dependence of the emission, we show that cavity leads to 250 K increase in the effective electronic temperature.

**Keywords**: infrared, HgTe, nanocrystals, photoluminescence, photonic cavity.

## INTRODUCTION

Semiconductor nanocrystals (NCs) offer unique, narrow, and tunable optical features. Due to these features, NCs have been singled out as particularly promising materials for the field of optoelectronics. Nevertheless, most of the initial applications of NCs were based on the optical pumping of the material, leading to the most mature technology being down converters for displays[1]. Certainly, the belief that the hopping mechanism for conduction in NCs films[2] and its inherently weak carrier mobility prevent efficient charge conduction has hindered the development of devices relying on charge transport. However, recent advancements in devices such as infrared imagers[3] or high current density-driven light-emitting diodes (LEDs)[4,5] have proven that such colloidal materials can be addressed electrically.

Despite these achievements, the goal of a NC-based electrically-pumped laser diode has yet to be achieved. For visible wavelengths, several necessary milestones toward this goal have already been reached, culminating in advanced heterostructure designs with a focus on Auger recombination, which has led to low lasing thresholds and population inversion in diode stacks[6].

This effort is still mostly lacking in the infrared. Significant efforts are conducted to make new material platform to emerge such as III-V semiconductors[7], but the focus is still on their synthesis rather than on coupling them to photonic structure, especially given their high sensitivity to oxidation. This is why to date, most of the efforts for infrared lasing using nanocrystals rely on PbS NCs[8,9]. Unfortunately, the strong degeneracy of the exciton in PbS NCs is highly unfavorable to population inversion, leading to insufficient performances. The only viable alternative in the infrared that is mature enough to reconcile high-quality colloidal growth and advanced device integration is HgTe. The material presents a reduced band edge degeneracy compared to PbS, and Geiregat *et al.* predict that HgTe NCs should display a low threshold for lasing, including upon electrical excitation[10]. However, demonstrations of stimulated emission from HgTe nanocrystals remain sparse[10,11].

A good way to promote population inversion and thereby stimulated emission in a material is its coupling to a photonic cavity. Again, very few works have been devoted to the coupling of HgTe NC emitters to photonic structures, and most of the effort has been focused on plasmonic metasurfaces[12–15]. The introduction of plasmonic metasurfaces has been successful primarily in magnifying the photoluminescence (PL) signal and gaining directivity to better outcouple emitted photons to the far field from LED stacks[16,17]. Nevertheless, this approach still suffers from two limitations. First, optical losses in the metal sometimes lead to exciton quenching. While this issue can be mitigated, as it has been shown that quenching is not an issue when the NCs are mutually coupled via Förster resonance energy transfer (FRET) and/or direct electronic coupling[18,19], the necessary conditions can be quite restrictive. Second, the same Joule losses limit the quality factor of resonant plasmonic structures, degrading their potential to enhance electric fields, and to reshape the PL both spectrally and spatially.

These reasons push toward the integration of the HgTe nano-emitters into dielectric cavities, as already proposed for a large variety of nano-emitters, including 2D materials[20], epitaxial quantum dots[21], defects in silicon[22], or even NCs[23–25]. In 2005, Heiss' group applied this principle by integrating HgTe NCs into a hybrid Bragg mirror/metallic mirror cavity[26].

We build on this concept and develop HgTe/CdS core-shell structures with an emission peak near telecom wavelengths. We unveil their carrier dynamics with resolution down to 35 fs, showing the presence of a nanosecond radiative emission together with a faster (20 ps) contribution appearing under high fluence and attributed to Auger relaxation. The material is then integrated onto various

substrates, including full dielectric mirror-based cavities. We systematically discuss the impact of the substrate on the PL spectrum, the field enhancement, the directivity, and the carrier dynamics.

## RESULTS AND DISCUSSION

We start by growing core-shell structured emitters in the short-wave infrared region. We choose to conduct our measurements using a material presenting a peak emission compatible with typical InGaAs sensors, as it allows for a more advanced characterization of the material using a microscopy setup. In particular, having a microscope coupled to a focal plane array enable the acquisition of dispersion map through the imaging of the back focal plane array. Furthermore, InGaAs detector also offer a high-resolution temporal resolution. This combination of imaging and fats response would have been partly prevented for longer wavelength materials. The material of interest is made of a quasi-spherical HgTe core on top of which a thin (1 monolayer) CdS shell is grown[27], as seen in the image in **Figure 1**a. The shell growth is obtained from the exposure of the core to cadmium bis(phenyldithiocarbamate) complex precursor[28]. Under mild temperature exposure, in presence of amine, the complex decompose into CdS. This high reactivity approach enables the growth of the shell in spite of a large lattice mismatch (around 10 % assuming 0.646 nm for HgTe and 0.5832 nm for CdS in zinc blende phase) and avoids exposing the core to high temperatures, as outlined in the methods. The obtained material presents an absorption band edge at 1300 nm, and a luminescence that peaks at 1450 nm, which in absolute value has a lower quantum yield (QY) comparted to the core (30 % of core PLQY). However, for the core only, we observe a continuous drop of the PL signal under excitation (Figure S1) which is highly detrimental when targeting the inclusion of the material into a cavity to maximize light excitation. The PL spectrum, which has a full width at half maximum (FWHM) of around 200 nm, as shown in **Figure 1**b., matches the imaging capability of traditional InGaAs sensors.

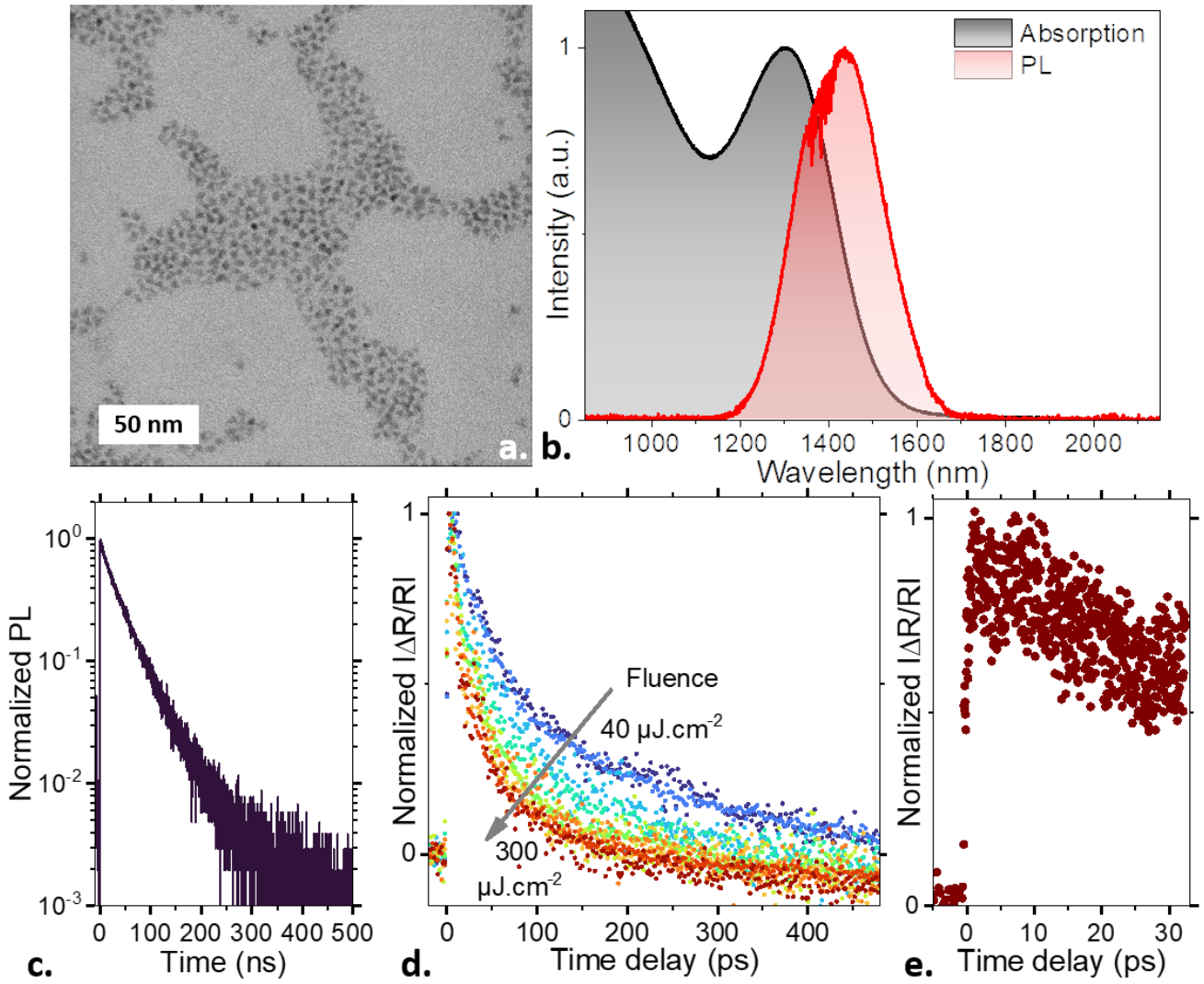


**Figure 1 Infrared nanocrystals**. a. TEM image of the HgTe/CdS NCs. b. Absorption and PL spectra from HgTe/CdS NCs. c. Time-resolved photoluminescence for a solution of HgTe/CdS NCs at 1500 nm. d. Transient reflectivity for pump (800 nm) and probe at 1500 nm for the material on sapphire under various fluence. e. Transient reflectivity at early time scale.

We then investigate the benefits of the shell on the optical properties of HgTe NCs. Indeed, the initial motivation for a core-shell structure has been to address the poor thermal stability of HgTe upon annealing[29], which leads to dramatic damage of the material used in infrared imagers even at moderate temperatures. Despite this, the benefit of the shell for PL characteristics is clearly highlighted by looking at the carrier dynamics. Time-resolved luminescence displays a quasi-mono exponential decay with a long decay time at around 30 ns, see **Figure 1**c. This clearly contrasts with core-only structures, both in terms of number of components and in terms of decay times. Indeed, core-only structures typically display complex decay curves with several components[17,30], while both core-only structures and previously reported core-shell structures[31] have typically much shorter decay times. In films, the dynamics speed up, reducing the PL decay time to 10 ns. This suggests the emergence of additional non-radiative pathways, as will be discussed later. Since the final purpose is to introduce the particles into a cavity with a high excitation rate, we anticipate a possible

emergence of Auger relaxation. There appears to be a disagreement on the characteristics of Auger relaxation for HgTe NCs, with some claims suggesting it is slow[31] and others suggesting it is fast[32].

To address this question, we conduct transient reflectivity measurements with 35 fs laser pulses, leading to an overall 50 fs resolution for the setup. Data at short time scales present a short rise time of the order of 800 fs (**Figure 1**e), which we attribute to the cooling of the electron from the pump-injected energy states (1.5 eV) down to the energy band edge (0.85 eV). This corresponds to a cooling rate of 0.8 $eV.ps^{-1}$, a value in the range of what has been reported for core only HgTe (0.36 $eV.ps^{-1}$ for small HgTe[33] NCs and 0.8 $eV.ps^{-1}$ for very large ones[34]). The transient reflectivity is then measured for increasing excitation fluences. At low fluence, there appears to be a single contribution in the hundreds of ps regime. As fluence is increased, a new contribution appears in the tens of ps regime, see **Figure 1**d. If we assume that the absorption cross section of the core-shell is barely affected by the introduction of the thin shell compared to that of the core[35], we can assume a cross section of $1.5x10^{-15}$ $cm^{-2}$. The emergence of the fast component above 100 $\mu J.cm^{-2}$ then corresponds to a fluence high enough to generate ≈1 carrier per NC. This makes reasonable the assumption to allocate the fast recombination mechanism to an Auger relaxation. An Auger decay of around 20 ps matches other measurements, as reported in previous studies[32,36], and lends credence to the fact that Auger mechanisms are fast in HgTe NCs. It is worth noting that there is no additional faster mechanism, see **Figure 1**e.

In the next step, we design a dielectric mirror (DM) with a stop-band that matches the PL emission range. The mirror is made of a combination of low and high refractive index materials, $SiO_2$ and $Ti_3O_5$ respectively. Both materials are chosen to be transparent, and thus lossless, in the spectral window of interest. The Bragg design for such a mirror consists of a periodic structure in which each layer has a $\lambda/4n$ thickness, with $\lambda$ being the central wavelength of the mirror's stop-band and $n$ the refractive index. The number of pairs in the mirror controls the magnitude of the reflectivity, while the index mismatch controls the bandwidth of the stop band. However, conventional periodic designs lead to poor control of the reflectivity magnitude outside of the stop band. In particular, the resulting transmission at 640 nm, the laser pump wavelength, is ≈ 75%, which is fairly low. Here, the pump laser wavelength is chosen in the visible so that the InGaAs detector used to characterize the photoluminescence (PL) is not sensitive to the excitation. To address this weak transmission in the visible, we change the design to an aperiodic structure (**Figure 2**a). This structure enables both a high reflectivity band in the 1400-1600 nm range which overlaps with the NCs' PL, and an anti-reflection band around 640 nm to maximize the transmission (up to 93%), as shown in **Figure 2**b. The resulting DM structure includes 15 layers (**Figure 2**a) and is 3 µm thick. In the visible, it appears as a partly transparent layer with a red aspect, as seen in **Figure 2**c. In the infrared, with a filter narrowing the spectral window to 1200-1700 nm, the DM clearly behaves as a mirror (**Figure 2**d), whereas the reference glass slide remains transparent.

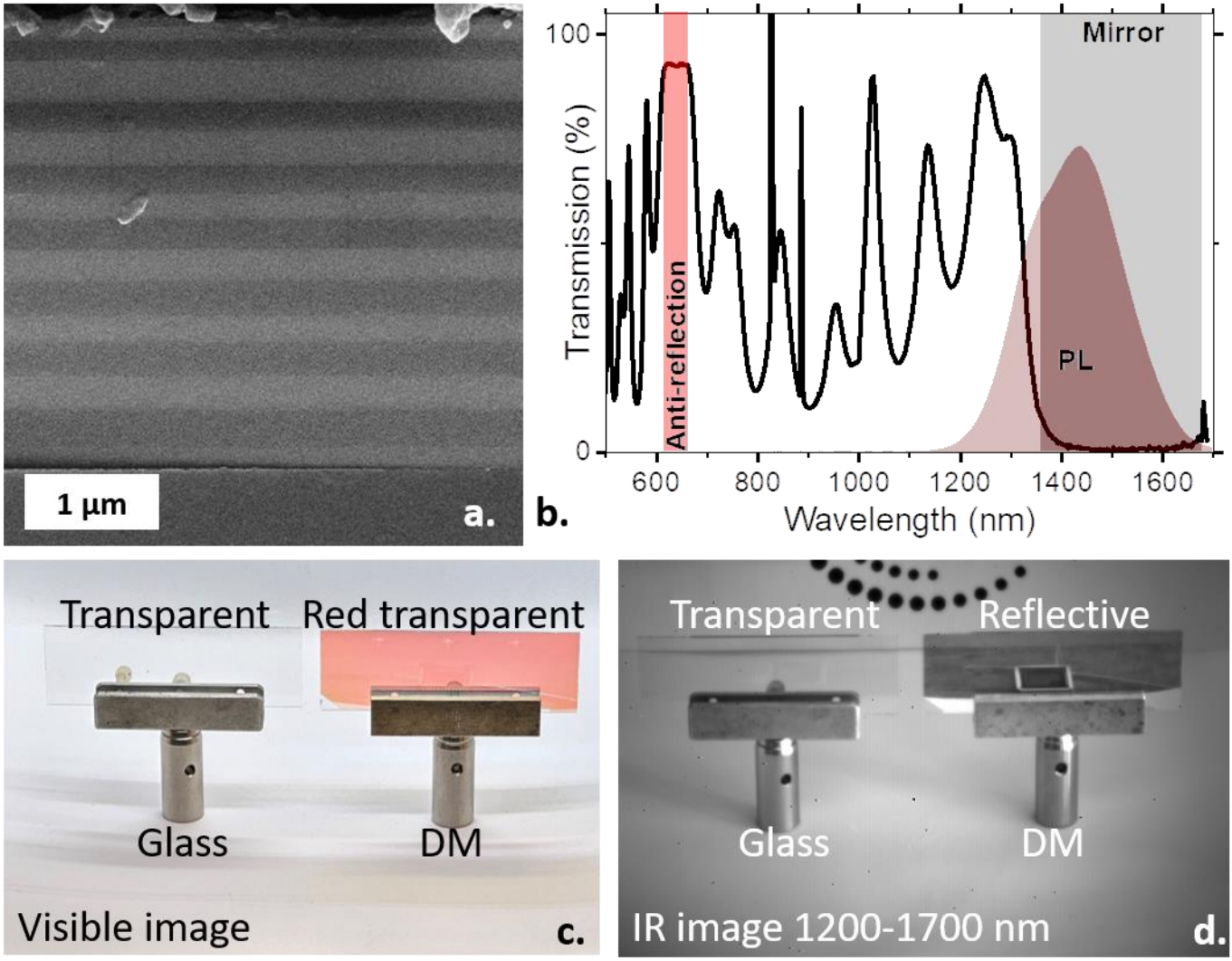


***Figure 2 Dielectric mirror from aperiodic stack*** *a. SEM cross section image of a $Ti_3O_5/SiO_2$ dielectric stack. b. Visible and short-wave infrared transmission of the stack depicted in a. The different points of interest are represented as shaded areas: the mirror stop-band optimized for the 1400-1600 nm range in grey, the PL range centered around 1450 nm in dark red, and the anti-reflective band around 640 nm in light red. c. Visible image of a glass slide and of the same slide functionalized with DM. d. Infrared image in the 1200-1700 nm range, showing that glass remains transparent, while DM coated glass slide is a mirror in this range.*

We then investigate, both experimentally and *via* simulations, in which ways the PL properties are affected by the choice of substrate. The NCs are deposited on glass, on gold (a lossy mirror), on a single DM (see the scheme as inset of **Figure 3**a), and in a cavity (i.e. sandwiched between two DMs, see the scheme as inset of **Figure 3**b). Mostly for mechanical considerations, the NCs are blended with PMMA, which acts as a transparent (Figure S3) medium that allows for thicker film deposition. In the cavity it also acts as glue to hold the two mirrors. The cavity is then further maintained by two metallic plates screwed together.

In Figure S2, we have simulated the field enhancement for each of the substrates and predicted an increase in the maximum value of the electric field inside the NC layer for different substrates. With respect to NCs on glass, the increase is of a factor around 4 for gold, 6 for a single DM, and 54

inside the dielectric cavity, suggesting a strong cavity effect. Both glass, gold, and single DM maintain a broad PL signal, as indicated by the dispersion map in **Figure 3**a and S4. It is also worth noting that the emission remains mostly non-dispersive. These results contrast with the case of the same material inside the cavity, as shown in **Figure 3**b, where the PL mode becomes narrow and dispersive. The narrowing of the PL is confirmed experimentally, as seen in **Figure 3**c and d. Typically, this translates into a drop of the FWHM from 200 nm to around 20 nm (12 meV). At this stage, it is important to check if this narrowing is the result of a spectral filtering resulting from the DM stack or actually induced by the cavity. In Figure S4 we compared the PL collected in two configurations: from the top of the mirror or through the mirror. The latter appears clearly blueshifted compared to the PL of the pristine material with no feature in the mirror stop band thus we can confidently attribute the narrowing of the peak to a cavity effect.

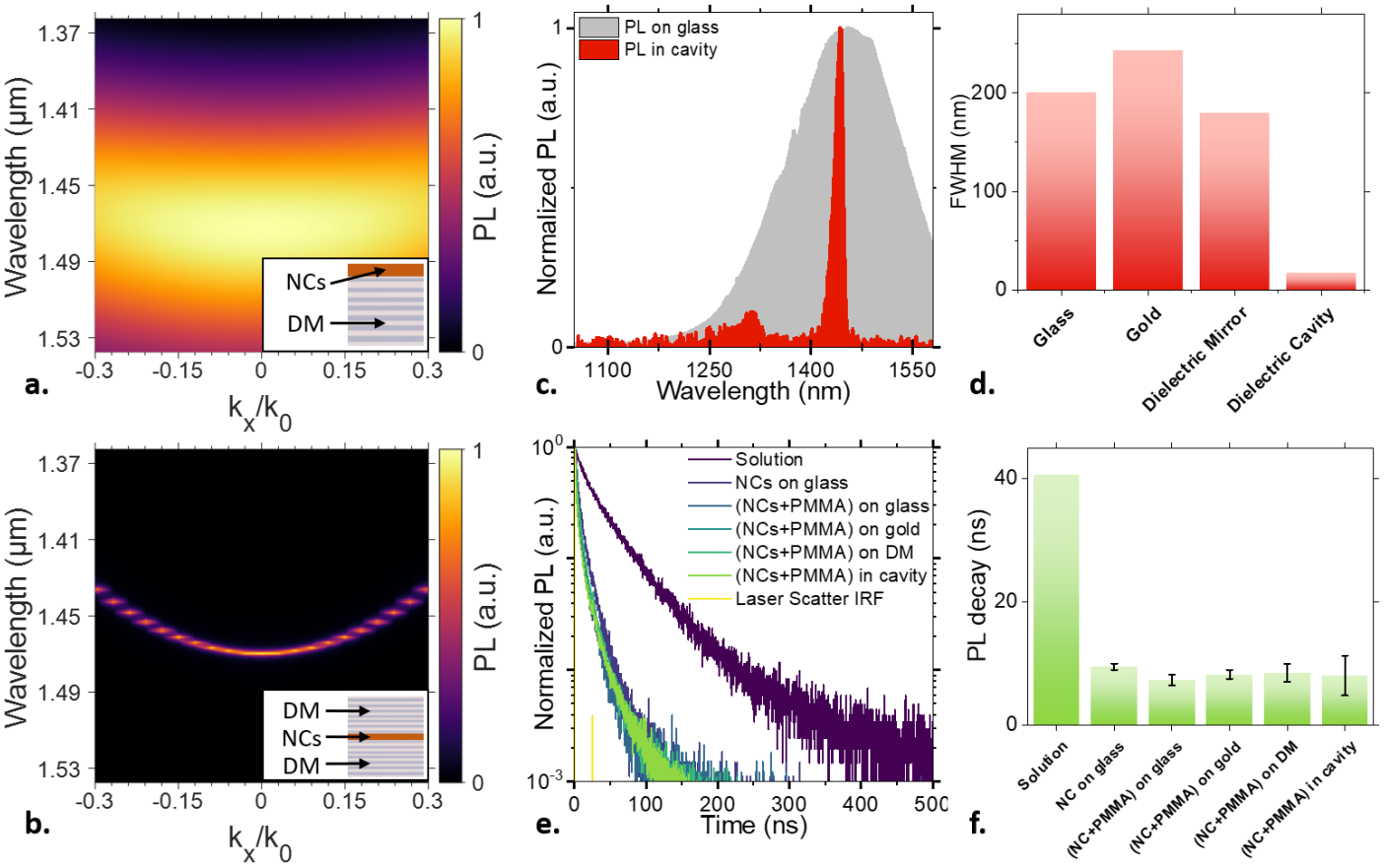


***Figure 3 Spectral shaping resulting from the cavity****. a. Simulated dispersion map (PL magnitude vs wavelength and in-plane wavevector) for NC film deposited on a single DM. The inset is a schematic of the NC film onto the DM. b. Simulated dispersion map for NC film inside a cavity. The inset is a schematic of the NC film between two DMs forming a cavity. c. Comparison of the PL spectra for HgTe/CdS NCs on glass and within the cavity. d. FWHM for the emission of HgTe/CdS NCs on various substrates. e. Time-resolved PL for HgTe/CdS NC solution and film deposited on various substrates at 1500 nm. f. PL decay time (time to reduce signal by a factor e) for HgTe/CdS NC solution and film deposited on various substrates.*

We also track the PL dynamics for the various substrates. We previously noted a clear acceleration as the material switches from the solution to the thin-film. However, the dynamics appear mostly unaffected by the chosen substrate, with decay times consistently around 10 ns, as shown in **Figure 3**d-e. This behavior aligns with what has been observed for PbS nanocrystals coupled to gold

metasurfaces[18], where the PL decay remains unaffected regardless of the nature of the metasurface due to very efficient FRET interactions among NCs. This behavior implies that if any enhancement of the PL occurs, it does throughout a change in the relative weight between the probability of non-radiative processes and the probability of radiative processes. This enhancement mechanism is very different from the Purcell effect, where the PL enhancement is due to a shortening of the photocarrier lifetimes. The presence here of a behavior incompatible with the Purcell effect is closely related to the fact that the nanocrystals are mutually interacting, making them behave as an effective semiconductor medium rather than a mere collection of individual emitters subject to the Purcell effect.

In addition to the spectral shaping, a second benefit of the cavity resides in its strong directivity. This is well illustrated by imaging the Fourier plane at different wavelengths, as shown in **Figure 4**, which reflects the directivity of the emission. On a gold substrate, the emission is omnidirectional, and the Fourier plane image reveals a homogeneous mapping regardless of wavelength. On a single DM (middle column of **Figure 4**a-b), the Fourier plane imaging reveals a slightly more intense signal at the center, reflecting the small dispersion of the band simulated by the dispersion map, see **Figure 3**a. For wavelengths corresponding to the PL signal on gold, the situation remains the same for various energies, although the amplitude changes. The cavity again reveals a different situation. The emission only covers a narrow range (consistent with the small FWHM of the PL signal), with no signal at 1400 or 1500 nm. The Fourier plane image now reveals a ring shape, as seen in the right part of **Figure 4**a-b, indicating emission along a 15° wide cone with a linewidth of ≈7°. Simulation nicely reproduces the measurement by tuning only the length of the cavity (*i.e.* the thickness of NCs), whereas the only material input is the optical index of the cavity medium taken equal to the optical index of PMMA due to the limited volume fraction of NCs.

The exact angular distribution at a given wavelength depends on the cavity length, and the Fourier backplane image can be modified from a single point (*i.e.,* normal emission) to a ring shape with an increase in thickness, as shown in Figure S5. Figure S5 also shows that the angular linewidth of the emission depends on the peak emission angle, with FWHM ranging from 12° at normal incidence down to 4° at a 15° angle. This result is consistent with the parabolic shape of the dispersion map simulated in **Figure 3**b. The capability of the cavity to emit light over a narrow angle window near the normal is not only interesting for laser cavity design but also for LEDs to address the issue of their poor light extraction efficiency.

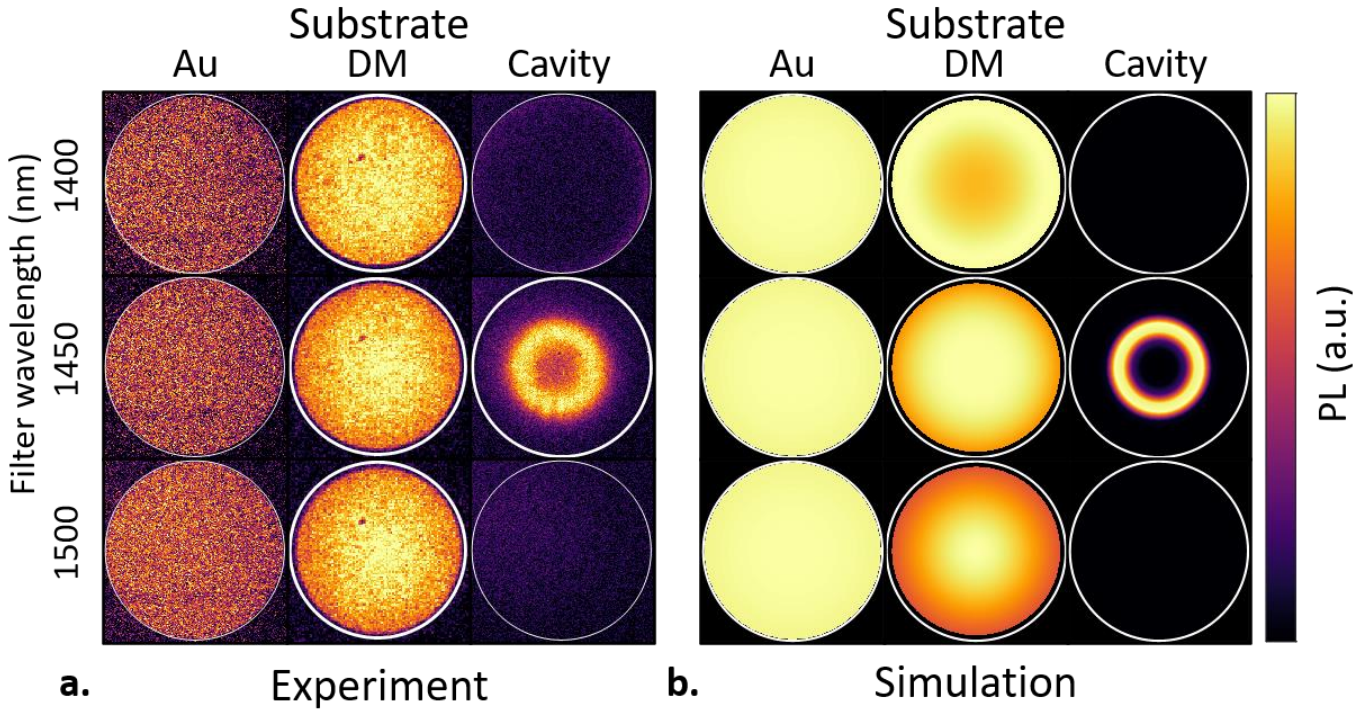


***Figure 4 Directivity of the emission inside a cavity****. a. Experimental mapping of the back focal plane array at three wavelengths around the cavity stop band and for three substrates (gold, single DM and cavity). The radius* $\sqrt{k_x^2 + k_y^2}/k_0$ *of the white circles is equal to 0.3. b. Simulation of the same dataset in part a. assuming a thickness of 110 nm.*

Finally, we studied the power dependence of the material under continuous wave (CW) excitation, for different substrates, as shown in **Figure 5**. On glass, we observed a clear increase in the PL magnitude together with a blue shift (20 nm on glass) and broadening on the high-energy side of the peak, as depicted in **Figure 5**a. Within the cavity, the power dependence of the spectrum appears even more drastic, as illustrated in **Figure 5**b. The low-power PL spectrum is mostly a single peak within the cavity stop band, as seen in **Figure 3**c. At increasing powers, we observe the emergence of additional features, presenting a very structured aspect. This new feature can be understood as the product of the blue-shifted PL by the transmission of the DM, as shown in **Figure 2**b. The more dramatic changes at high energy in the cavity then imply a stronger blue-shift than on glass for the same excitation power.

The power dependence behavior can be rationalized using the local Kirchhoff law[19,37–39], which claims that the emission signal of a collection of mutually interacting emitters is the product of the absorption at the emitted wavelength by Planck's law $PL(\lambda) \propto A(\lambda)\, W(\lambda,T_e)$, with $T_e$ as the electronic temperature. The Wien approximation of Planck's law leads to $W(\lambda,T_e) = 2hc^2\lambda^{-5}\exp[-hc/(\lambda k_B T_e)]$, where h and $k_B$ are the Planck and Boltzmann constants, and λ is the photon wavelength. As a result, there is a value of $T_e$ that should make the quantity $PL(\lambda)/W(\lambda,T_e)$ a similar spectrum for all operating conditions.

$$PL(P_i, T_e) = PL(P_O, T_0) \times \left( \frac{e^{\frac{hc}{\lambda k_B T_e}}}{e^{\frac{hc}{\lambda k_B T_0}}} \right) \quad (1)$$

An example of this renormalization procedure is provided in **Figure 5**c, which allows the extraction of the effective temperature of the electrons, assuming that for low excitation power, the electrons are thermalized at room temperature, see Figure S6. We observe that with the CW source used in this setup, the increase in temperature remains modest for glass, gold, and the single DM (less than 50 K). On the other hand, in the cavity the elevation of temperature can be as high as 250 K (**Figure 5**d), suggesting a strongly out-of-equilibrium operation. Note, however, that the temperatures may be overestimated due to band-filling effects at high pumping fluences [40,41]. This behavior is consistent with the increased electric field in the cavity compared to other substrates (Figure S2) and further reinforces that the observed shaping of the PL is not the result of PL filtering through the DM stack

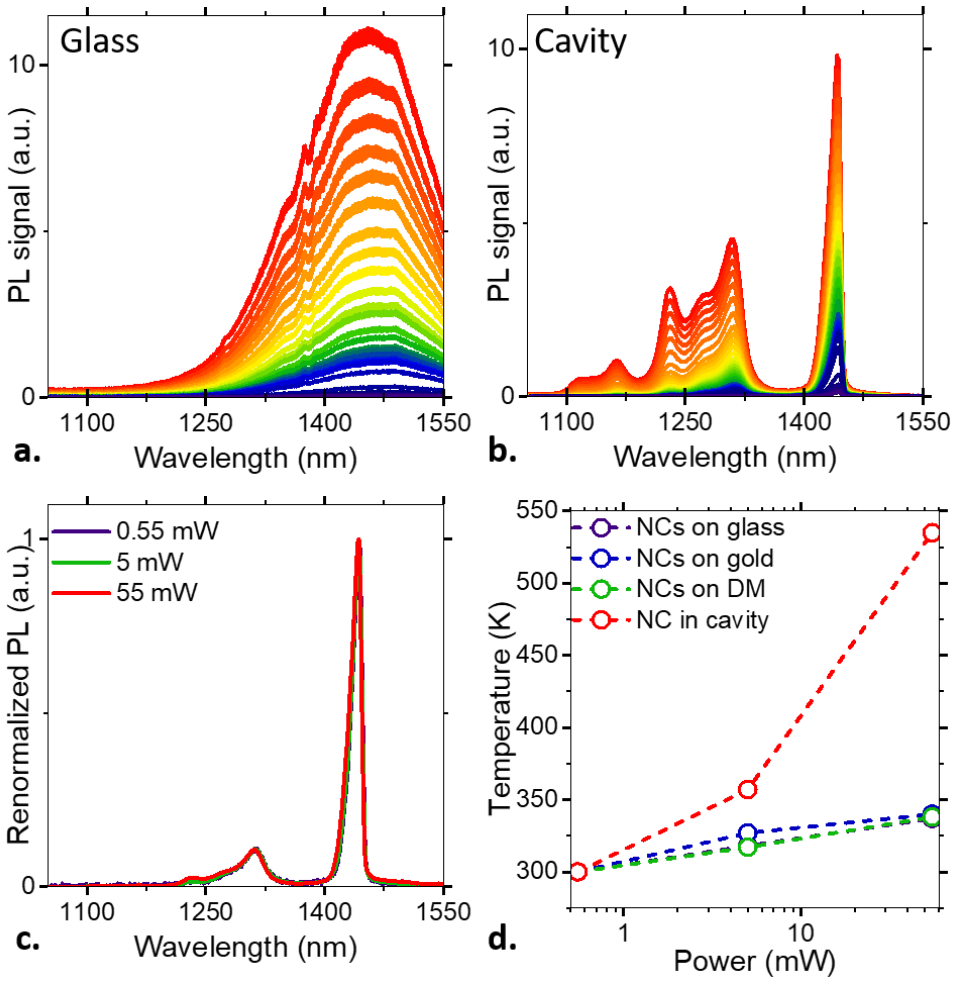


***Figure 5 Power dependence for material inside the cavity****. a. PL spectra for HgTe/CdS NCs on glass under various incident laser powers (at 640 nm) spanning from 0.5 mW to 50 mW. The apparent discontinuities around 1360 nm are caused by absorption lines of the atmosphere. b. PL spectra for HgTe/CdS NCs inside the cavity under various incident laser powers (at 640 nm) spanning from 0.5 mW to 50 mW. c. Renormalized data set from part b. using the local Kirchoff law procedure. d. Extracted equivalent electronic temperature for the NC deposited on various substrate, assuming that at low power the temperature matches the room temperature.*

## CONCLUSION

A core-shell HgTe/CdS structure was successfully grown. The structure exhibits clear benefits for PL, with an extended PL lifetime compared to the core-only structure, reaching 120 ns in solution (30 ns in film) for emission at 1450 nm. However, under high fluence, the Auger relaxation in the 20 ps regime is probably still too fast to expect the observation of lasing with quasi-CW pumping. Future efforts will require further engineering of the electron-electron scattering rate through the design of heterostructures. The large energy offset and lattice mismatch between HgTe and CdS are not favorable, and an intermediate layer with a suitable lattice constant and band gap is likely to extend the biexciton lifetime.

The coupling of infrared NCs to a dielectric cavity leads to drastic spectral reshaping with a tenfold narrowing of the PL linewidth, which is now narrower than $k_BT$. It also considerably narrows the emission angle, bringing it closer to the normal of the mirror. The power dependence of the spectrum shows that the cavity brings the electrons further away from equilibrium, with an effective temperature 250 K above the one resulting from the film on glass under the same excitation condition. However, the cavity does not affect the carrier dynamics suggesting that NCs inside the cavity cannot be considered as individual emitters. The benefits brought by the cavity appear highly appealing for a transfer to LED designs as both the spectral and the spatial reshaping of the emission are promising for improved light extraction efficiency.

## SUPPORTING INFORMATION

Supporting Information include details about (*i*) method, (*ii*) benefit of core shell for PL, (*iii*) filtering using DM stack, (*iv*) field enhancement map, (*v*) correlation between cavity thickness and directivity and *(vi*) Renormalized power dependence using the local Kirchoff law procedure.


## ACKNOWLEDEGMENTS

We thank Xiang Zhen Xu for performing TEM imaging and Paola Atkinson for periodic Bragg mirror growth. H.Z. thanks the Chinese Scholarship Council for PhD funding. D.B. acknowledges the financial support from the French Department of Defense (DGA). XL thanks Renatech network for support. The project is supported by ERC grants Ne2dem (grant 853049), Forward (grant n° 771688) and AQDtive (grant n°101086358). This work was supported by French state funds managed by the Agence Nationale de la recherche (ANR) through the grant Copin (ANR-19-CE24-0022), Frontal (ANR-19-CE09-0017), Graskop (ANR-19-CE09-0026), Bright (ANR-21-CE24-0012), MixDFerro (ANR-21-CE09-0029), Quicktera (ANR-22-CE09-0018), Operatwist (ANR-22-CE09-0037) and E-map (ANR-22-CE50) and as part of the “Investissements d’Avenir” program (Labex NanoSaclay, reference: ANR-10-LABX-0035). Work performed at the Center for Nanoscale Materials, a U.S. Department of Energy Office of Science User Facility, was supported by the U.S. DOE, Office of Basic Energy Sciences, under Contract No. DE-AC02-06CH11357.


## CONFLICT OF INTEREST

The authors declare no competing financial interest.

## REFERENCES


1. Shu, Y. *et al.* Quantum Dots for Display Applications. *Angewandte Chemie* **132**, 22496–22507 (2020).

2. Ledos, N. *et al.* Stop Blaming Hopping Conduction in Nanocrystal Arrays, Use it for Active Photonics! *Adv Mater Technol* 2301463 (2024) doi:10.1002/ADMT.202301463.

3. Gréboval, C. *et al.* Photoconductive focal plane array based on HgTe quantum dots for fast and cost-effective short-wave infrared imaging. *Nanoscale* **14**, 9359–9368 (2022).

4. Ahn, N. *et al.* Electrically driven amplified spontaneous emission from colloidal quantum dots. *Nature* **617**, 79–85 (2023).

5. Jung, H. *et al.* Two-band optical gain and ultrabright electroluminescence from colloidal quantum dots at 1000 A $cm^{-2}$. *Nat Commun* **13**, 3734 (2022).

6. Diroll, B. T., Hua, M., Guzelturk, B., Pálmai, M. & Tomczak, K. Long-Lived and Bright Biexcitons in Quantum Dots with Parabolic Band Potentials. *Nano Lett* **23**, 11975–11981 (2023).

7. Bahmani Jalali, H., De Trizio, L., Manna, L. & Di Stasio, F. Indium arsenide quantum dots: an alternative to lead-based infrared emitting nanomaterials. *Chemical Society Reviews* vol. 51 9861–9881 Preprint at https://doi.org/10.1039/d2cs00490a (2022).

8. Taghipour, N. *et al.* Low-Threshold, Highly Stable Colloidal Quantum Dot Short-Wave Infrared Laser enabled by Suppression of Trap-Assisted Auger Recombination. *Advanced Materials* **34**, 2107532 (2022).

9. Whitworth, G. L., Dalmases, M., Taghipour, N. & Konstantatos, G. Solution-processed PbS quantum dot infrared laser with room-temperature tunable emission in the optical telecommunications window. *Nat Photonics* **15**, 738–742 (2021).

10. Geiregat, P. *et al.* Continuous-wave infrared optical gain and amplified spontaneous emission at ultralow threshold by colloidal HgTe quantum dots. *Nat Mater* **17**, 35–42 (2017).

11. Diroll, B. T., Dabard, C., Lhuillier, E. & Ithurria, S. Band Edge Excitons and Amplified Spontaneous Emission of Mercury Chalcogenide Nanoplatelets. *Adv Opt Mater* 2302004 (2023) doi:10.1002/ADOM.202302004.

12. Sergeeva, K. A. *et al.* Laser-Printed Plasmonic Metasurface Supporting Bound States in the Continuum Enhances and Shapes Infrared Spontaneous Emission of Coupled HgTe Quantum Dots. *Adv Funct Mater* **33**, 2307660 (2023).

13. Sergeev, A. A. *et al.* Tailoring spontaneous infrared emission of HgTe quantum dots with laser-printed plasmonic arrays. *Light Sci Appl* **9**, 16 (2020).

14. Bossavit, E. *et al.* Plasmon-Assisted Directional Infrared Photoluminescence of HgTe Nanocrystals. *Adv Opt Mater* **11**, 2300863 (2023).

15. Dabard, C. *et al.* Electroluminescence and Plasmon-Assisted Directional Photoluminescence from 2D HgTe Nanoplatelets. *Journal of Physical Chemistry C* **127**, 14847–14855 (2023).

16. Qu, J. *et al.* Electroluminescence from nanocrystals above 2 µm. *Nat Photonics* **16**, 38–44 (2021).

17. Qu, J. *et al.* Electroluminescence from HgTe Nanocrystals and Its Use for Active Imaging. *Nano Lett* **20**, 6185–6190 (2020).

18. He, P. *et al.* Observation of Quasi-Invariant Photocarrier Lifetimes in PbS Nanocrystal Assemblies Coupled to Resonant and Nonresonant Arrays of Optical Antennas. *ACS Photonics* **11**, 437–444 (2024)

19. Wang, H. *et al.* Revisiting the Role of Metallic Antennas to Control Light Emission by Lead Salt Nanocrystal Assemblies. *Phys Rev Appl* **10**, 034042 (2018).

20. Knopf, H. *et al.* Integration of atomically thin layers of transition metal dichalcogenides into high-Q, monolithic Bragg-cavities: an experimental platform for the enhancement of the optical interaction in 2D-materials. *Opt Mater Express* **9**, 598–610 (2019).

21. Peter, E. *et al.* Exciton-photon strong-coupling regime for a single quantum dot embedded in a microcavity. *Phys Rev Lett* **95**, 067401 (2005).

22. Lefaucher, B. *et al.* Purcell Enhancement of Silicon W Centers in Circular Bragg Grating Cavities. *ACS Photonics* **11**, 24–32 (2024).

23. Guzelturk, B., Kelestemur, Y., Olutas, M., Delikanli, S. & Demir, H. V. Amplified spontaneous emission and lasing in colloidal nanoplatelets. *ACS Nano* **8**, 6599–6605 (2014).

24. Mariano, F. *et al.* The enhancement of excitonic emission crossing Saha equilibrium in trap passivated $CH_3NH_3PbBr_3$ perovskite. *Commun Phys* **3**, 41 (2020).

25. Bertucci, S. *et al.* High Quality Factor in Solution-Processed Inorganic Microcavities Embedding $CsPbBr_3$ Perovskite Nanocrystals. *ACS Applied Optical Materials* **1**, 1343–1349 (2023).

26. Roither, J., Kovalenko, M. V., Pichler, S., Schwarzl, T. & Heiss, W. Nanocrystal-based microcavity light-emitting devices operating in the telecommunication wavelength range. *Appl Phys Lett* **86**, 241104 (2005).

27. Zhang, H. *et al.* Infrared Imaging using thermally stable HgTe/CdS nanocrystals. *Submitted*.

28. Frederick, M. T. & Weiss, E. A. Relaxation of exciton confinement in CdSe quantum dots by modification with a conjugated dithiocarbamate ligand. *ACS Nano* **4**, 3195–3200 (2010).

29. Zhang, H. *et al.* Material Perspective on HgTe Nanocrystal-Based Short-Wave Infrared Focal Plane Arrays. *Chemistry of Materials* **34**, 10964–10972 (2022).

30. Keuleyan, S., Kohler, J. & Guyot-Sionnest, P. Photoluminescence of mid-infrared HgTe colloidal quantum dots. *Journal of Physical Chemistry C* **118**, 2749–2753 (2014).

31. Zhang, W. H., Yang, J. & Yu, J. S. Synthesis of stable near-infrared emitting HgTe/CdS core/shell nanocrystals using dihydrolipoic acid as stabilizer. *J Mater Chem* **22**, 6383–6388 (2012).

32. Sergeeva, K. A. *et al.* Ultrafast Charge Carrier Dynamics and Transport Characteristics in HgTe Quantum Dots. *Journal of Physical Chemistry C* **126**, 19229–19239 (2022).

33. Ruppert, M. *et al.* Intraband dynamics of mid-infrared HgTe quantum dots. *Nanoscale* **14**, 4123–4130 (2022).

34. Apretna, T. *et al.* Few picosecond dynamics of intraband transitions in THz HgTe nanocrystals. *Nanophotonics* **10**, 2753–2763 (2021).

35. Lhuillier, E., Keuleyan, S. & Guyot-Sionnest, P. Optical properties of HgTe colloidal quantum dots. *Nanotechnology* **23**, 175705 (2012).

36. Melnychuk, C. & Guyot-Sionnest, P. Slow Auger Relaxation in HgTe Colloidal Quantum Dots. *Journal of Physical Chemistry Letters* **9**, 2208–2211 (2018).

37. Greffet, J. J., Bouchon, P., Brucoli, G. & Marquier, F. Light Emission by Nonequilibrium Bodies: Local Kirchhoff Law. *Phys Rev X* **8**, 021008 (2018).

38. Caillas, A., Suffit, S., Filloux, P., Lhuillier, E. & Degiron, A. Identification of Two Regimes of Carrier Thermalization in PbS Nanocrystal Assemblies. *Journal of Physical Chemistry Letters* **12**, 5123–5131 (2021).

39. Bailly, E. *et al.* 2D Silver-Nanoplatelets Metasurface for Bright Directional Photoluminescence, Designed with the Local Kirchhoff's Law. *ACS Nano* **18**, 4903–4910 (2024)

40. Nguyen, D. T. *et al.* Quantitative experimental assessment of hot carrier-enhanced solar cells at room temperature. *Nat Energy* **3**, 236–242 (2018).

41. Esmaielpour, H. *et al.* Investigation of the spatial distribution of hot carriers in quantum-well structures via hyperspectral luminescence imaging. *J Appl Phys* **128**, 165704 (2020).

*Supporting information for*

# Shaping the infrared luminescence of colloidal nanocrystals using a dielectric microcavity

Erwan Bossavit[1,2$], Huichen Zhang[1$], Nicolas Ledos[1], Mariarosa Cavallo[1], Dario Mastrippolito[1], Leonardo Curti[3], Adrien Khalili[1], Albin Colle[1], Pierrick Lample[4,5] Mateusz Weis[4], Florent Margaillan[1], Xavier Lafosse[6], Yoann Prado[1], Emmanuel Péronne[4], Debora Pierucci[1], Sandrine Ithurria[3], Davide Boschetto[4], Benjamin T. Diroll[7], Aloyse Degiron[8], Emmanuel Lhuillier[1*]

[1] Sorbonne Université, CNRS, Institut des NanoSciences de Paris, INSP, F-75005 Paris, France.
[2] Synchrotron SOLEIL, L'Orme des Merisiers, Départementale 128, 91190 Saint-Aubin, France.
[3] Laboratoire de Physique et d'Etude des Matériaux, ESPCI-Paris, PSL Research University, Sorbonne Université, CNRS UMR 8213, 10 rue Vauquelin 75005 Paris, France.
[4] LOA, ENSTA Paris, Ecole Polytechnique, CNRS, Institut Polytechnique de Paris, 181 Chemin de la Hunière et des Joncherettes 91120 Palaiseau, France.
[5]Université Paris-Saclay, CEA, CNRS, LIDYL, Gif-sur-Yvette, 91191, France
[6]Centre de Nanosciences et de Nanotechnologies, CNRS, Université Paris-Saclay, C2N, Palaiseau 2110, France.
[7] Center for Nanoscale Materials, Argonne National Laboratory, 9700 S. Cass Avenue, Lemont, Illinois 60439, United States.
[8] Université de Paris, CNRS, Laboratoire Matériaux et Phénomènes Quantiques, 75013 Paris, France.

$ these two authors have equal contributions

*To whom correspondence should be sent: el@insp.upmc.fr

## Table of content

# 1. METHODS

**Chemicals:** Mercury bromide ($HgBr_2$, Alfa Aesar), cadmium chloride ($CdCl_2$, Alfa Aesar, 99.99%), tellurium powder (Te, Alfa Aesar, 99.99%), trioctylphosphine (TOP, thermofisher scientific, 90%), oleylamine (OLA, Acros, 80-90%), octadecene (ODE, Acros Organics, 90%), dodecanethiol (DDT, Sigma-Aldrich, 98%), methanol (MEOH, Carlo Erba, 99.8%), acetone (VWR), absolute ethanol (EtOH, VWR), isopropanol (IPA, VWR), toluene (Carlo Erba, 99.3%), N,N dimethylformamide (DMF, VWR), 2-mercaptoethanol (MPOH, Merck, >99%), 3-mercaptopropionic acid (MPA, Alfa Aesar, 99%), poly(methyl methacrylate) (PMMA, Atuglass), Anisole (Alfa Aesar, 99%).. All chemicals are used as received, except oleylamine which is centrifuged before used. **Mercury compounds are highly toxic. Handle them with special care.**

**Ammonium phenyldithiocarbamate synthesis ($NH_4PDTC$)[1,2]:** In a 3-neck 100 mL flask under nitrogen bubbling at room temperature, equipped with a trap of NaClO, 25 mL of $NH_4OH$, 25 mL acetone and aniline (10 mL, 0.11 mol) were introduced and cooled down with an ice bath. Then, $CS_2$ (10 mL, 0.16 mol) was added dropwise with vigorous stirring. The solution turned red after 5 minutes, and a pale-yellow crystalline product slowly precipitated over the following 90 minutes. The product was collected by vacuum filtration and washed 4 times with $CHCl_3$. The $NH_4PDTC$ was dried under vacuum and stored in a freezer to prevent decomposition.

**Cadmium bis(phenyldithiocarbamate) synthesis [$Cd(PDTC)_2$][1] :** In an Erlenmeyer flask, $NH_4PDTC$ (600 mg, 3.2 mmol) was dissolved in 50 mL water. The solution was clear yellow. Then, $Cd(NO_3)_2.4H_2O$ (493 mg, 1.6 mmol) was dissolved in 40 mL water and added dropwise to the flask over 5 minutes, leading to immediate precipitation of $Cd(PDTC)_2$ as a pale yellow powder. The product was collected by centrifugation, and washed with 25 mL of cold absolute ethanol. The precipitate was dried under a Schlenk line and stored in a desiccator.

**1 M TOP:Te precursor**: 6.35 g of Te powder was mixed in 50 mL of TOP in a three-neck flask. The flask was kept under vacuum at room temperature for 5 min and then the temperature was raised to 100 °C. Furthermore, degassing of the flask was conducted for the next 20 min. The atmosphere was switched to Ar and the temperature was raised to 275 °C. The solution was stirred until a clear orange coloration was obtained. The flask was cooled down to room temperature and the color switched to yellow. Finally, this solution was transferred to a nitrogen-filled glove box for storage.

**HgTe core with 7000 $cm^{-1}$ (1.45 µm) band edge:** In a 50 mL three-neck flask, 18 mL of oleylamine was degassed under vacuum at 110℃ for 1 h. Then the atmosphere was switched to $N_2$ and the temperature was set at 120℃. Meanwhile, in a 20 mL vial, 144 mg (0.4 mmol) of $HgBr_2$ was dissolved in 5 mL of oleylamine under sonication and degassed at 110℃ for 30 min. Then, the solution in vial was cooled down to room temperature and switched to $N_2$ atmosphere. 0.3 mL of TOP:Te (1 M) with 20 µL (0.23 mmol) of 3-mercaptopropanoic acid (MPA) was injected into the vial. The solution was injected into the hot oleylamine in the flask through a syringe. After 1 min, the reaction was quenched with 1 mL of a solution of DDT in toluene (10% v/v) and ice bath. The flask content was transferred to a falcon and was precipitated by adding MeOH and centrifugation. The pellet was redispersed in toluene. The nanocrystals were precipitated a second time with absolute EtOH and redispersed in toluene. The toluene solution was centrifugated to remove the unstable phase and then filtered with 0.2 µm PTFE filter. This material is used for PL to ensure that the signal matches our time-resolved detection capability.

**Spherical shell growth:** 18 mg $CdCl_2$ was added to 18 mL of a 50% (v/v) oleylamine-octadecene solution in a flask and was degassed at 110°C for 30 min. The mixture was then cooled down to 40°C and switched to $N_2$ atmosphere. 3.5 mL of HgTe core solution (0.45 OD at 400 nm after a 500x dilution) was introduced to the flask, and 3 cycles of vacuum/$N_2$ cycles were conducted. $Cd(PDTC)_2$ (50 mg, 1 mmol) in 1.5 mL of a 30% (v/v) oleylamine-octadecene mixture was then injected at 40°C quickly, and the flask was heated up to 80°C for 2 min. The reaction was quenched by injecting 2 mL of a 10% (v/v) DDT/OA-toluene solution and cooling

down to room temperature. The content in the flask was transferred to a centrifuge tube and precipitated with EtOH. The pellet was redispersed in toluene and then precipitated again with IPA. After redispersion, the toluene solution was centrifugated to remove the unstable phase (the supernatant was kept).

**Dielectric mirror deposition**: The top side of the glass is coated with an optimized interferential filter made of 15 alternating titanium pentoxide ($Ti_3O_5$, Neyco,99.99% ) and silicon dioxide ($SiO_2$, Neyco, 99.99%) thin layers starting with $Ti_3O_5$, with a total thickness of 2.998 µm. These layers have been deposited by ion beam assisted e-beam evaporation (IBAD MEB 800, Plassys). Ion assistance is provided by an End Hall ion gun (eH1000 source, Kaufman & Robinson KRI). The design, synthesis, and refinement of the custom coating have been performed theoretically with a commercial software (Essential MacLeod, Thin Film Center Inc.).

$SiO_2$ and $Ti_3O_5$ (denoted as L and H for low and high refractive indices materials respectively) have been chosen because of their transparency in the considered spectral ranges but also for their refractive index contrast ($n_L$= 1.460 ± 0.012 at λ=642 nm and $n_L$= 1.453 ± 0.018 at λ=1550 nm whereas $n_H$=2.464 ± 0.053 at λ=642 nm and $n_H$=2.309 ± 0.080 at λ=1550 nm).

Conventional Bragg reflectors consisting of alternate quarter wavelength optical thicknesses (QWOT) whose reference wavelength is 1550 nm, provides a poor anti-reflective behavior (R≈25%) at shorter wavelengths in the visible range (630-650 nm). The optical thicknesses have been thus optimized to match the desired specifications ($R_{max}$ around λ=1550 nm and $R_{min}$ around λ=642 nm) leading to a stack denoted as $H(LH)^7$.

Both $Ti_3O_5$ and $SiO_2$ were evaporated at a rate of 0.25 nm·s$^{-1}$. Starting materials are 1 to 3 mm pieces of $Ti_3O_5$ and $SiO_2$ put in molybdenum liners. The background pressure in the chamber was $1.0 \times 10^{-7}$ mbar, and the working pressure was $\approx 3.0 \times 10^{-4}$ mbar with flows of 10 standard cubic centimeters per minute (sccm) of Ar and 10 sccm of $O_2$ for the ion source, and 10 sccm of Ar for the keeper (plasma bridge neutralizer). Discharge currents were set to 1.6 A and 2 A during $Ti_3O_5$ and $SiO_2$ deposition steps respectively. Under those conditions the ion source discharge voltage was 150 V and 75 V during $Ti_3O_5$ and $SiO_2$ deposition steps respectively. The optical thicknesses were followed in real time using both a quartz microbalance and an in-situ spectroscopic ellipsometer (M2000, J.A. Woolam) at 60.5° of incidence.

The actual deposited stack for each layer of $H(LH)^7$ starting from glass, was: 153.4 nm ($Ti_3O_5$)/258.0 nm ($SiO_2$)/225.0 nm ($Ti_3O_5$)/232.3 nm ($SiO_2$)/183.4 nm ($Ti_3O_5$)/233.4 nm ($SiO_2$)/ 211.5 nm ($Ti_3O_5$)/207.4 nm ($SiO_2$)/163.7 nm ($Ti_3O_5$)/190.0 nm ($SiO_2$)/220.4 nm ($Ti_3O_5$)/193.8 nm ($SiO_2$)/266.3 nm ($Ti_3O_5$)/134.1 nm ($SiO_2$)/125.4 nm ($Ti_3O_5$).

**HgTe/CdS film deposition*:*** Different substrates (glass, gold-coated silicon, Bragg-mirror-coated glass, Bragg-mirror-coated GaAs) were briefly washed by spraying ethanol and then were dried with $N_2$. To obtain thick NC films (> 100 nm) while preserving the PL of the NCs, the pristine solution was mixed with PMMA. A commercially available solution of PMMA in anisole was diluted by adding anisole until a 200 nm film was obtained after spin-coating at 4000 rpm for 30 s. The pristine QD solution was mixed with the diluted PMMA solution in a 2:1 ratio by volume. This solution was then spin-coated onto the various substrates at 2000 rpm for 45 s. The thickness of the obtained films was measured to be ≈ 200 nm using a profilometer (Dektak 150). For the full Bragg cavity, a second Bragg-mirror-coated glass substrate was deposited on top of the first after the NC film deposition, with the two Bragg-mirror-coated surfaces facing each other. The full cavity was then held in place mechanically using two metal plates tightened together with screws.

**Transmission electron microscopy:** For TEM imaging, a drop of diluted NCs solution is casted on a copper grid covered with an amorphous carbon film. The grid is degassed overnight under secondary vacuum. A JEOL 2010F is used at 200 kV for the acquisition of pictures.

**Infrared photoluminescence spectroscopy**: A vial containing a solution of NCs is illuminated by a blue flash light. This light is used as a source of an FTIR (Thermo Scientific Nicolet iS50) operated in rapid scan mode. The beamsplitter is made of $CaF_2$ and the signal collected using an extended InGaAs detector (2.6 µm cut-off uncooled). The spectra are generally averaged 256 times and acquired with a 4 $cm^{-1}$ resolution.

**Infrared microscopy**: The images of the spatial distribution of the photoluminescence in the Fourier space were obtained with a BX51WI upright microscope from Evident/Olympus coupled to an InGaAs camera cooled at -10°C (model Xeva 1M with 320x256 pixels from Xenics) via a Bertrand lens (focal length 30 mm) and a Telan lens (focal length 20 mm). Bandpass filters were inserted in the optical path to image the photoluminescence in the Fourier plane at selected wavelengths, as indicated in the figures. The microscope objective used in these experiments was a 10X LMPLN10XIR objective from Evident/Olympus (NA =0.3). The samples were excited through the same objectives with the light originating from a 640 nm Picoquant laser diode (LDH-IB-640-B) operated in continuous wave mode. A dichroic mirror (Thorlabs DMLP950R) was used to separate the pump from the photoluminescence signal.

The photoluminescence spectra were acquired with an IX73 inverted microscope from Evident/Olympus coupled to a spectrometer composed of an Isoplane160 monochromator and a PyLoN Linear InGaAs photodiode array from Teledyne Princeton Instruments. The pumping and collection scheme was the same as for the Fourier plane imaging experiments described in the previous paragraph: a 10X LMPLN10XIR objective from Evident/Olympus was used to both excite the samples optically and to collect the photoluminescence. The excitation light was provided by a 640 nm Picoquant laser diode (LDH-IB-640-B) operated in continuous wave mode. A dichroic mirror (Thorlabs DMLP950R) was used to separate the pump from the photoluminescence signal.

**Time-resolved photoluminescence measurements:** Time-resolved photoluminescence measurements of samples in solution (hexanes), or in solid films, were performed using a ≈35 fs 640 nm pump (≈1 $\mu J \cdot cm^{-2}$) generated using an optical parametric amplifier from a Ti:sapphire fundamental. Photoluminescence was collected by an optical fiber and directed through a monochromator to a superconducting nanowire array. To collect many spots from the samples, they were translated within the same plane of the excitation/collection.

**Transient reflectivity at ultra short time scale:** Time-resolved reflectivity with sub-100 fs time resolution has been carried out by a commercial laser system from Coherent company working at 1 kHz repetition rate, delivering pulses centered at 800 nm and energy of 1.5 mJ per pulse. The pulses are split into two paths, where one is used as pump pulse, while the other one as probe pulse. A motorized delay line allows the control of the time delay between the pump and probe pulses. The probe pulse is injected into an optical parametric amplifier (TOPAS C from Light Conversion company), in order to tune the wavelength between 1.2 and 2.4 microns. We used an optical chopper at 0.5 kHz, in order to detect only pump-induced changes in the transient reflectivity. The optical chopper has an external phase control of the rotation, which allows an optimal synchronization with the laser pulse train. The signal is measured by a photodiode connected to a lock-in amplifier (SR830 from Stanford Research Systems). The lock-in is set at the frequency of the pump pulse, i.e. 0.5 kHz, in order to detect only the pump-induced changes in the reflected signal. We selected a pump pulse wavelength centered at 800 nm, while the probe pulse is centered at 1500 nm. The pump pulse is focused on 800 microns at the sample surface, while the probe pulse is focused on 200 microns in order to ensure the probing of a uniformly excited surface. The pump is P-polarized and the probe is S-polarized.

However, no dependence on polarization has been found on these samples, mainly due to the random crystallographic orientation of the quantum dots.

**Infrared absorption spectroscopy:** A Fourier transform infrared spectrometer (FTIR) Fischer Nicolet iS50 in attenuated total reflection (ATR) configuration is used. The source is a white halogen lamp, the beamsplitter is made of $CaF_2$ and the detector is a DTGS ATR. Spectra are typically acquired with a 4 $cm^{-1}$ resolution and averaged over 32 spectra.

**Visible absorption spectroscopy:** spectra are acquired using a solution of NCs within a glass cuvette and measured using a Jasco 730 double path spectrometer with a 1 nm resolution.

**Electromagnetic simulation**: The optical properties of the structures are simulated using the finite element method (FEM) software COMSOL Multiphysics, *2D Frequency Domain Interface*. A Floquet periodicity is set as the boundary conditions for the edges on the left and right of the model. Two periodic ports are placed away from the structure on either side, separated from the main structure by 20 µm of either substrate or air to avoid nonphysical interferences. One of the ports turns on the wave excitation while the other turns it off. The direction of the incoming wave is then determined by which port is "on". The top-most and bottom-most regions are defined as perfectly matched layers to absorb outgoing waves and minimize possible nonphysical reflections due to the limited model size.

The total thickness of air and substrate was chosen to be 30 µm to avoid nonphysical interferences. The thickness of the different oxide layers for the dielectric mirror was obtained from optical ellipsometry and confirmed by SEM observation. The thickness of the NC layer was left as an adjustable parameter.

The relevant optical property of the materials, the complex optical index, is obtained: from COMSOL's built-in database for glass and air; from a Drude model for gold; from optical ellipsometry for the NC layer and the different oxide layers that make up the dielectric mirror.

A physics-controlled mesh is enabled with extremely fine element size.

The reflectance (resp. the transmittance) of the structure is determined by integrating the absolute value of the time-averaged power outflow over a boundary placed behind the "on" port (resp. behind the "off" port) and dividing by the input power defined in the port. The dissipated power per unit volume in the metals and nanocrystals can be calculated using the formula $P = -0.5\omega|F|^2 Im(\varepsilon)$, where $F$ is the electric field, $\omega$ is the angular frequency of the incident wave, and $Im(\varepsilon)$ is the imaginary part of the material permittivity. The absorption of one material is calculated by integrating the dissipated power over the volume of the material, and then by dividing by the incident power defined in the port. Finally, the angular dispersion of the photoluminescence can be simulated using the reciprocity principle between near-field excitation and far-field emission[3]: the far-field emission from the structure with integrated incoherent emitters is reciprocal to the intensity of the near-field excited in the structure by the incident external light averaged over the position of the emitters. Thus:

$$P(\theta, \phi; \lambda) \propto P_i(\lambda) \times \iiint_V |E(\theta, \phi; \lambda; r)|^2 \, d^3r$$

where $P(\theta,\phi;\lambda)$ is the power emitted from the structure in the direction $(\theta,\phi)$, at wavelength $\lambda$, $P_i(\lambda)$ is the power emitted at wavelength $\lambda$ by a single emitter (obtained from the measurement of the PL of NCs in solution), V is the volume of NCs, and $E(\theta,\phi;\lambda;r)$ the local electric field in position r excited by a plane wave of wavelength $\lambda$, and incident along the direction $(\theta,\phi)$ (obtained from solving Maxwell's equations using COMSOL). Since all studied structures are axisymmetric along the direction normal to the surface, it is assumed $P(\theta,\phi)$ is independent of $\phi$ and $P(\theta)$ is calculated for a single value of $\phi$.

## 1. Benefit from Core shell for PL measurments

The used shell is thin, first because it was designed to be compatible with detector and thick shell appears highly detrimental to carrier mobility. Thin character of the shell also results from the large lattice mismatch (10%) between the CdS and HgTe, making thick shell growth even more challenging. As a result, the PL of the core shell is only 30 % of the one of the core. However, the improved thermal stability prevents the continuous drop in the PL magnitude, together with a blue shift, that we observe for core only, see Figure S 1. This lack of stability was quite a problem for the PL characterization. With the core shell, we observe an increase in PL magnitude over the same period of time.

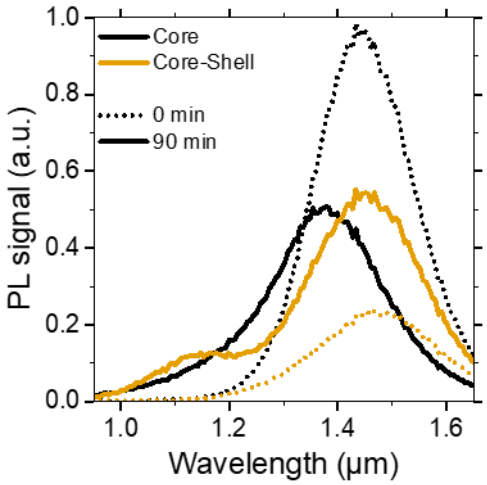


***Figure S 1 Benefit of core shell on PL**. PL spectrum for core and core shell (same absorption) at time 0 and after 90 min of excitation with under 100 mW of light at 640 nm*

## 2. Field enhancement maps

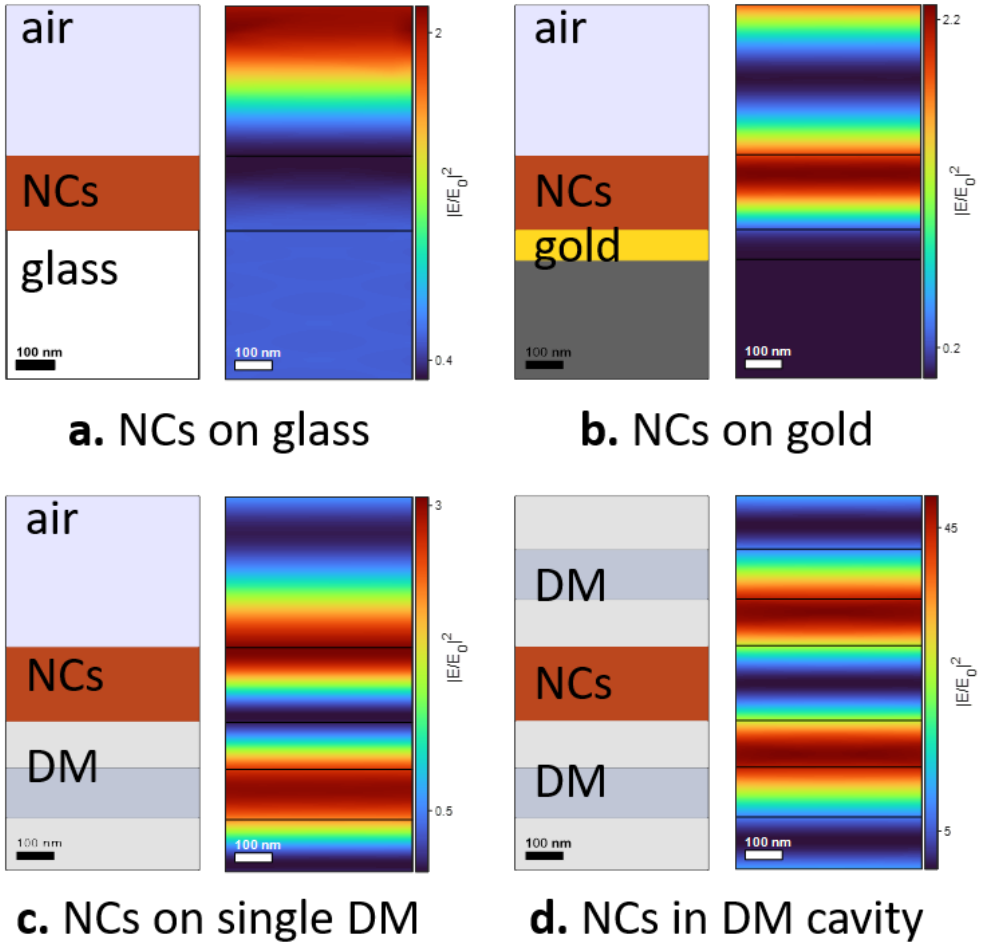


***Figure S 2 Impact of substrate on field enhancement****. Left is a sketch of the simulated structure combining substrate and NCs film, while right is the squared amplitude of the electric field for the corresponding structure. a. NCs on glass. b. NCs on gold. c. NCs on a single DM. d. NCs in a dielectric cavity.*

## 3. Filtering effect from the DM stack

Given PMMA is used as material to glue the cavity, it is critical to check it transparency in the spectral range of interest, see **Figure S 3**. **Figure S 3**a presents the infrared absorption of a thick PMMA layer, showing that absorption remains weak below 1.6 µm. **Figure S 3**b depicts the absorption from pristine PMMA and HgTe blended in PMMA, showing that in this case similar to the cavity case, the PMMA absorption remains marginal.

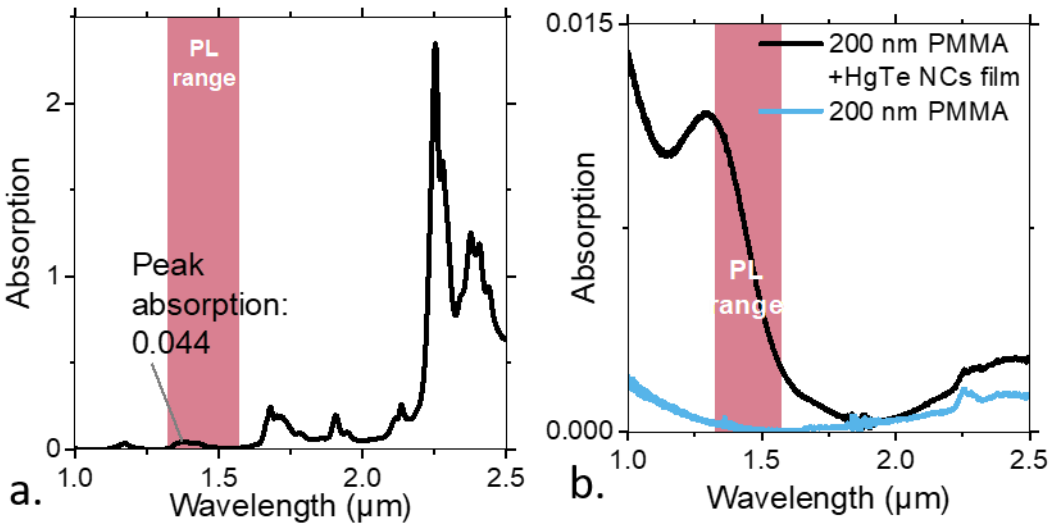


***Figure S 3 Absorption from PMMA in the spectral range of interest****. a. Absorption spectrum from a 600 μm thick film of PMMA. b. Absorption spectra from a 200 nm thick PMMA layer, and from the same layer blended with HgTe at concentration used in cavity.*

Spectral narrowing from the PL may also result from the filtering of the DM stack, this it is critical to discriminate if the narrowing effect is actually resulting from a cavity effect. To do so we have collected the PL either from the top of the mirror or through the mirror, see **Figure S 4**. PL collected from the top of the mirror, where DM acts as mirror matches the one from PL on glass. Reversely the PL collected through the mirror is clearly blueshifted toward wavelengths below the mirror stop-band and no narrow PL is observed in the mirror stop band.

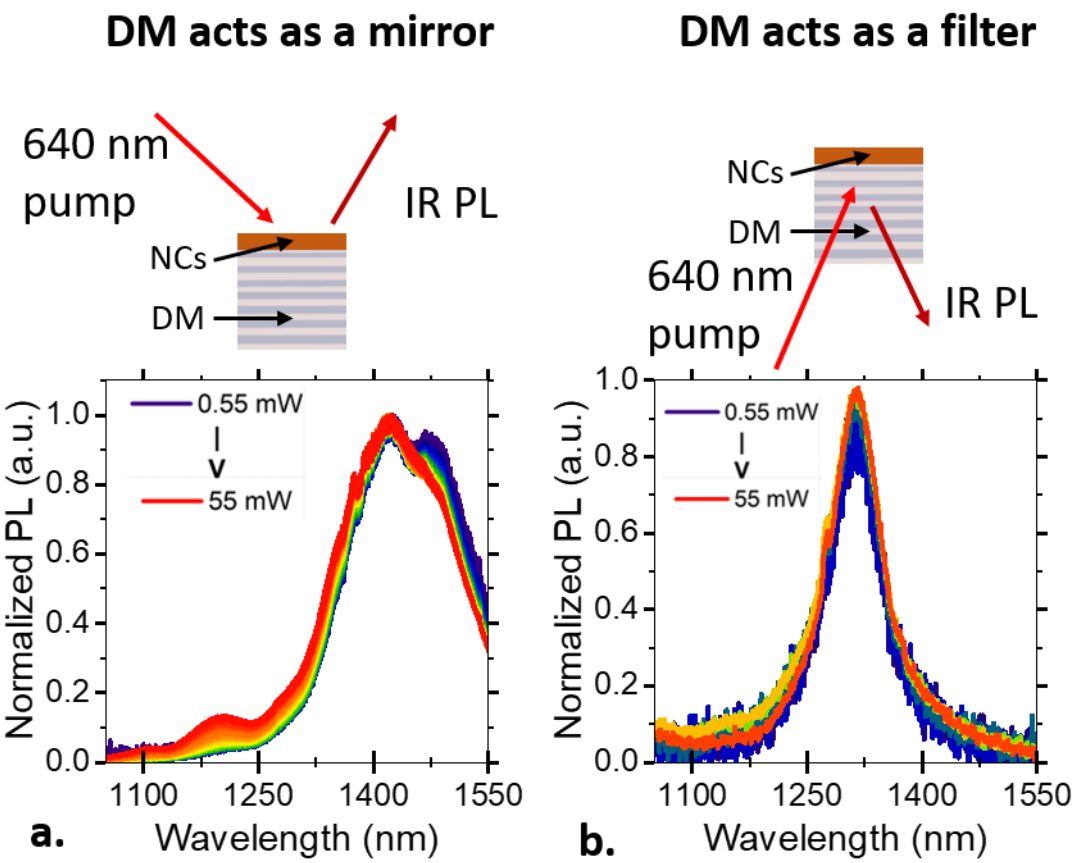


***Figure S 4 mirror vs filtering effect of the DM structure****. a. PL spectra under various irradiance while the NCs on DM are excited from the top, making the DM acting as a mirror. b. PL spectra under various irradiance while PL is connected through the DM that acts as a filter.*

## 4. Correlation between thickness and directivity

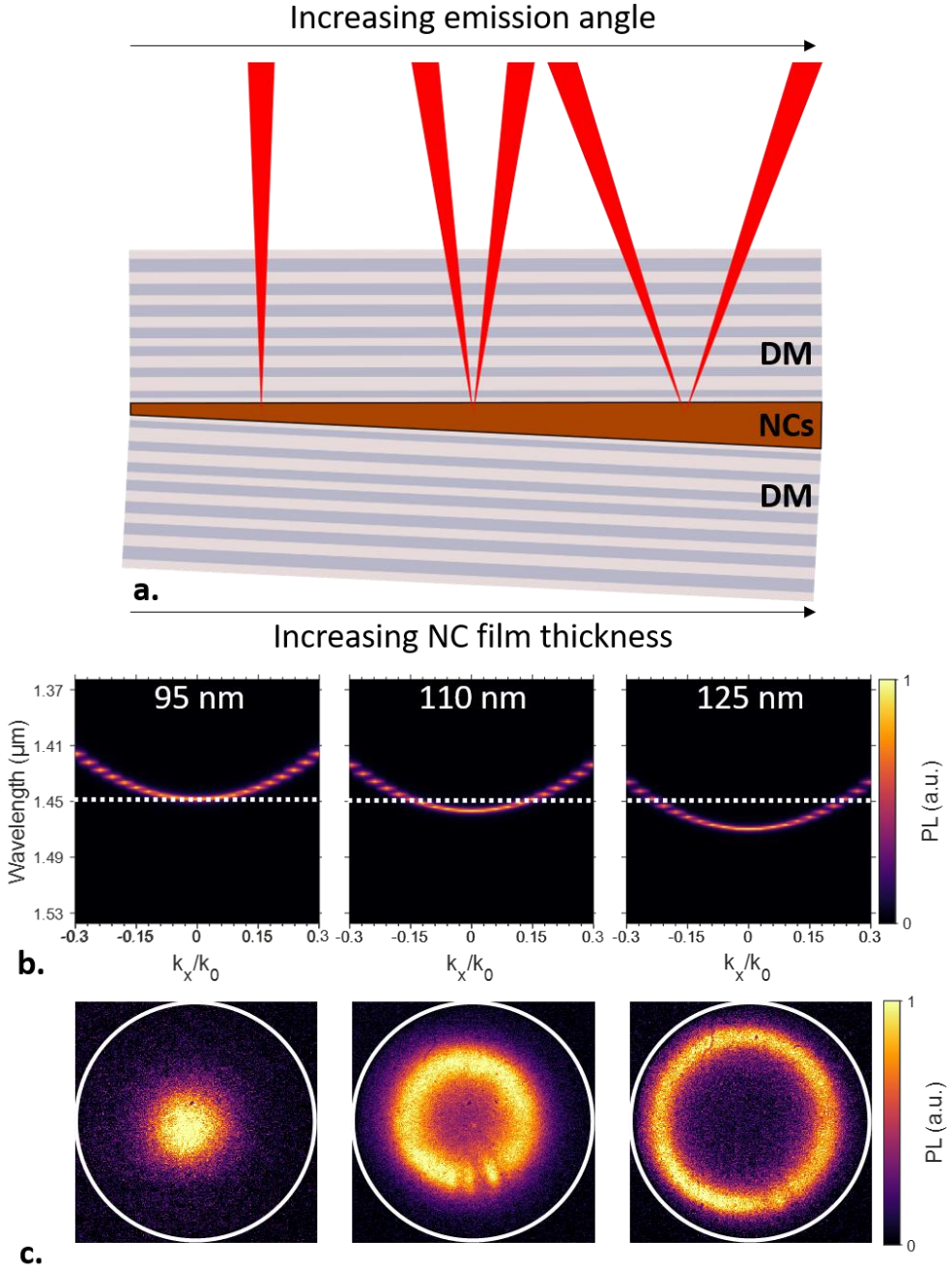


***Figure S 5 Relation between cavity thickness and directivity****. a. Schematic of the cavity formed between the two DM in the presence of a small angle. b. PL dispersion maps for the NCs in the cavity while the thickness of the cavity is tuned. Thicker cavities red shift the PL signal. c. Fourier plane imaging through a filter at 1450 nm for three different spots of the cavity. The small tilt induces a change of thickness in the cavity and thus a change of the emission angle for a given wavelength. The radius* $\sqrt{k_x^2 + k_y^2}/k_0$ *of the white circles is equal to 0.3.*

## 5. Kirchoff's law applied to emission on various substrate

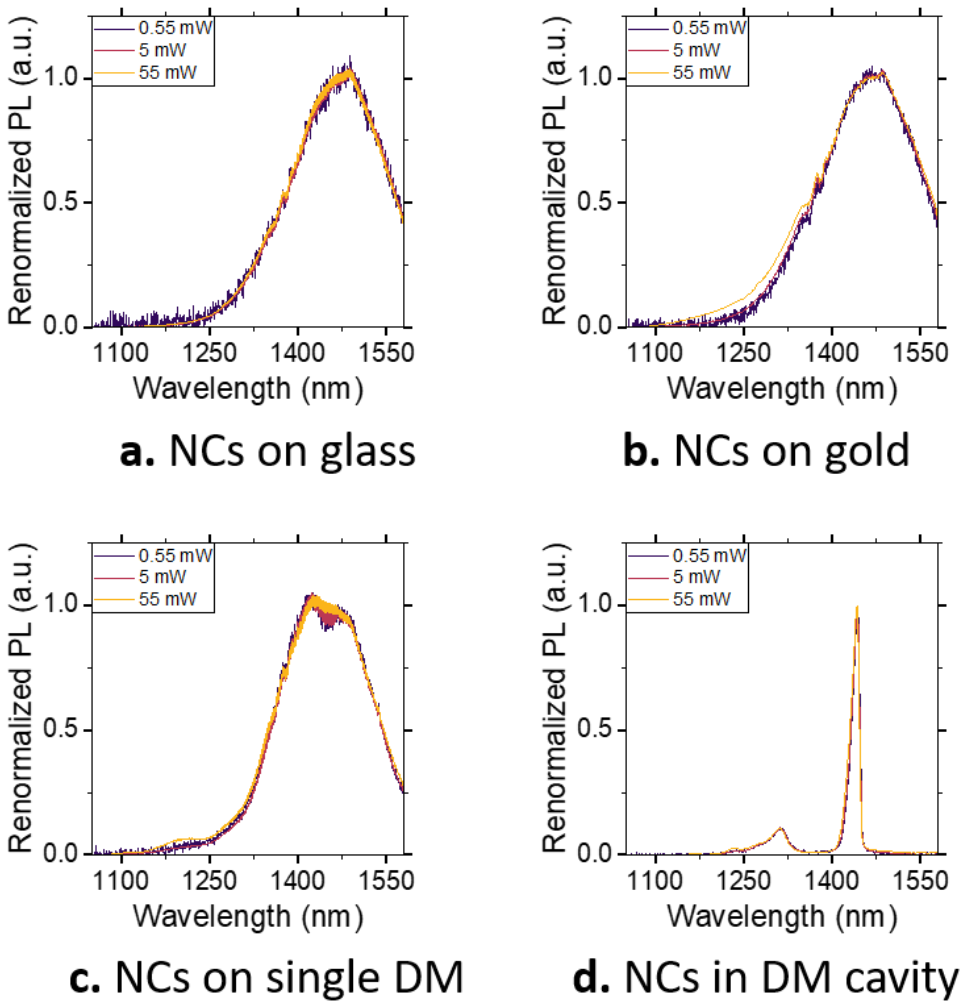


***Figure S 6 Renormalized power dependence using the local Kirchoff law procedure****. a. for NCs on glass. b. for NCs on gold. c. for NCs on single DM. d. for NCs in cavity.*

## 6. References


(1) Kamath, A., Melnychuk, C. & Guyot-Sionnest, P. Toward Bright Mid-Infrared Emitters: Thick-Shell n-Type HgSe/CdS Nanocrystals. *J. Am. Chem. Soc.* **143**, 19567–19575 (2021).

(2) Frederick, M. T. & Weiss, E. A. Relaxation of Exciton Confinement in CdSe Quantum Dots by Modification with a Conjugated Dithiocarbamate Ligand. *ACS Nano* **4**, 3195–3200 (2010).

(3) Vaskin, A., Kolkowski, R., Koenderink, A. F. & Staude, I. Light-emitting metasurfaces. *Nanophotonics* **8**, 1151–1198 (2019).